Inverse scattering for rotationally scanned optical coherence tomography

Daniel L. Marks, Tyler S. Ralston, P. Scott Carney, and Stephen A. Boppart

Beckman Institute of Advanced Science and Technology, 405 North Mathews Avenue, Urbana, Illinois 61801

Optical coherence tomography of luminal structures, such as for intravascular or gastrointestinal imaging, is performed by using a fiber-optic catheter as a beam-delivery probe. The interrogating beam is scanned angularly by rotating the fiber around a fixed central axis. Because the beam is focused only at a fixed distance from the center of the fiber, only scatterers near this distance are resolved. We present a solution of the inverse scattering problem that provides an estimate of the susceptibility of the sample for an angularly scanned Gaussian beam focused at a fixed distance from the origin. This solution provides quantitatively meaningful reconstructions while also extending the volume of the sample that is resolvable by the instrument. © 2006 Optical Society of America

OCIS codes: 100.3010, 110.4500.

1. INTRODUCTION

The utility of noninvasive and minimally invasive medical imaging techniques, such as optical coherence tomography[1,2] (OCT), is determined in large part by the degree to which the images provide a unique view or contrast with diagnostic value. Although OCT can achieve micrometer-scale resolution, it has a limited penetration depth of $1-2$ mm. This depth limits the application of OCT to external tissue surfaces unless minimally invasive techniques are used. Fiber-optic OCT catheters have been integrated with endoscopes to image the esophagus, colon, and other internal organs and mucosal tissue.[3–11] In these instruments, the illumination originates inside the object or tubular lumen being imaged, and is usually scanned azimuthally around the long axis of the catheter. As the catheter is azimuthally scanned and translated along the long axis of the catheter, a three-dimensional (3-D) image of the object is acquired. Because the beam is typically focused at a fixed distance from the catheter, the depth of focus of the resulting images is confined to a narrow annulus. In previous work[12] we developed a method to resolve scatterers outside of the focus by solving the inverse scattering problem for the case that the beam direction is fixed and the central position of the beam is scanned over a two-dimensional (2-D) plane. In this paper, we analyze the inverse scattering problem for the azimuthally and longitudinally scanned catheter. The relationship between the object susceptibility and the acquired OCT reflectance data is derived, a simulation is performed to demonstrate the potential utility of the algorithm, and the resolution is found for various values of the imaging system parameters.

An endoscope, used to explore the tubular lumens within the human gastrointestinal tract, typically consists of a long, flexible device of 1 cm diameter or less. Inside the endoscope, in addition to white-light illumination and CCD imaging optics, are working channels through which various instruments for biopsy or manipulating tissue are passed. For example, tissue biopsy samples can be extracted and withdrawn by forceps or suction. Smaller-diameter catheters are used in the cardiovascular system, e.g., for the insertion of balloons for angioplasty or to deploy stents.[13] Intravascular catheters minimize invasiveness and provide access to vascular lesions associated with cardiovascular disease.

Image guidance is an important application of catheter-based imaging. While many surgical procedures utilize external imaging methods such as x-ray computed tomography and magnetic resonance imaging, integrated image guidance simplifies the apparatus because external registration is not required. Additionally, such external imaging methods are expensive and some may expose the patient to ionizing radiation. Ultrasound transducers have been integrated into catheters, but the resolution is limited by the relatively long wavelength of sound waves in aqueous media. Catheter-based OCT imaging is used for image guidance, for *in vivo* diagnosis, and possibly for prognostic assessment.[14] For example, OCT has been used to identify potentially dangerous arterial plaques and lipid pools in the coronary artery.[15] The appeal of catheter-based OCT is its combination of small size, high resolution, and imaging speed for minimally invasive imaging.

OCT operates by illuminating the object with a focused, broadband beam. The backscattered light is collected, and by using interferometric detection, the time delay and therefore the distance along the beam to scatterers inside the object are determined. By scanning the beam through the object, the locations of scatterers in three dimensions can be found. The resolution of OCT in the axial direction, along the direction of propagation of the beam, is determined primarily by the bandwidth of the light source. However, the resolution in the transverse direction is not constant along the beam. At the focus of the beam, the resolution is determined by the focused spot size, but away from the focus the resolution degrades because the

beam is diverging or converging. This loss of resolution is usually assumed to be an inevitable consequence of defocus.

In previous work, we showed that, after solution of the inverse scattering problem, the transverse resolution of scatterers in the unfocused region is the same as the resolution of scatterers at the focus. More specifically, we derived a set of equations connecting the structure of the sample with the OCT data. We then obtained an analytic solution of these equations and developed a set of computer algorithms based on that solution. The algorithms produce reconstructions with a uniform resolution equal to that seen in the focus of the unprocessed data.[12] That analysis was for the case in which the beam orientation is fixed and the position of the central axis of the beam is translated on a 2-D linear Cartesian grid to obtain an image. The improvement in resolution for the out-of-focus regions was effected by treating the data as input to an inverse scattering problem based on the physics of OCT imaging. In a similar manner, this paper addresses the inverse scattering problem for OCT, but for the case of an azimuthally scanned catheter rather than the lateral translation as in the earlier paper. We show that features may be resolved by computed reconstruction outside the focus, thus extending the region in which features can be visualized, and potentially improving our ability to detect changes that are clinically significant.

In this work, the OCT catheter design considered is one where a focused beam is directed perpendicular to the catheter. Typically these catheters consist of a single-mode optical fiber, a focusing lens (typically a graded-index lens cemented or fused to the fiber), and a right-angle prism or a custom cleaved surface for reflecting the beam by 90 deg to the side of the catheter. An illustration of this design is given in Fig. 1. By rotating the catheter about its long axis, the beam may be directed along any path perpendicular to the axis. By pushing or pulling the catheter, the beam is translated along the long axis of the catheter. Together these two degrees of freedom enable the instrument to scan a cylindrically shaped volume around the catheter. Typical imaging with this catheter design involves acquisition of axial scans (either in the time or frequency domain) while rotating the catheter through 360 deg, advancing the catheter a small distance along its long axis, and then repeating the measurement.
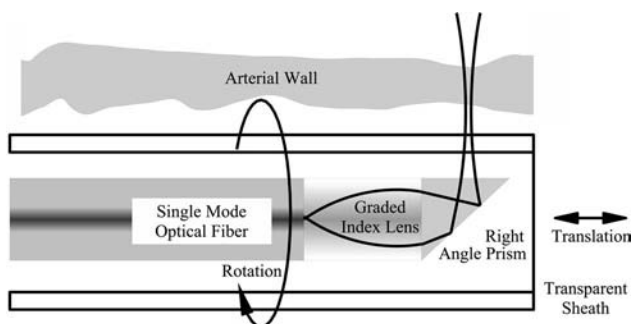

Fig. 1. Diagram of an OCT catheter. A single-mode fiber guides an optical signal, which is focused into a converging beam by the lens. The prism directs the beam at a right angle to the catheter. The beam is scanned azimuthally, rotating around the long axis of the catheter and is translated along the long axis of the catheter to collect cylindrical 3-D volumes of data.

After acquisition, one possesses a data set parameterized by the illumination frequency (or time delay), the angular coordinate of the catheter during the scan, and the translational position of the catheter along its axis. With our solution of the inverse problem, we infer the object susceptibility from these data.

We note that a similar synthetic aperture imaging problem also arises when imaging with ultrasound catheters[16] because some ultrasound catheters employ angularly scanned focused beams. A related inverse problem common to synthetic aperture imaging is the inversion of reflectance data from spherical averages.[17–21] The following analysis differs in that it addresses the finite NA Gaussian beam, rather than approximating the Gaussian beam by a spherical wave. Other approaches to inversion of data from focused ultrasound beams include the virtual source method,[22] which uses the synthetic aperture focusing technique to form the image.[23,24] These methods do not provide a quantitatively meaningful solution of the inverse scattering problem in the way our method does. Additionally, this solution to the inverse scattering problem also may have computational speed advantages when combined with fast inverse Radon transform techniques and fast Fourier transforms, rather than the backprojection- and backpropagation-based image formation methods.

2. FORWARD PROBLEM

This work draws heavily on a previous paper[12] in which the inverse problem for OCT with a linearly scanned Gaussian beam is developed. In the previous paper, the Gaussian beam is translated in a straight line perpendicular to its axis, rather than being rotated about the origin.

We consider an experiment in which a Gaussian beam originates at a position with Cartesian coordinates $(0, p, 0)$. Let us denote Cartesian coordinates fixed relative to the sample by $\mathbf{r} = (x, y, z)$, and let us denote Cartesian coordinates fixed relative to the beam by $\mathbf{r}' = (x', y', z')$. For each fixed axial position of the fiber, $y = y' = p$. The beam is directed at an angle θ from the z axis and along the z' axis. The coordinates may be related by a rotation matrix $\mathbf{R}(\theta)$ so that $\mathbf{r} = \mathbf{R}(\theta)\mathbf{r}'$ where

$$\mathbf{R}(\theta) = \begin{bmatrix} \cos\theta & 0 & \sin\theta \\ 0 & 1 & 0 \\ -\sin\theta & 0 & \cos\theta \end{bmatrix}. \tag{1}$$

The beam is focused a distance z_0 from the y axis. The field is polychromatic with power spectrum $A^2(k)$ where $k = \omega/c$ is the wavenumber associated with frequency ω. The width of the beam waist is a function of frequency given by $W(k) = \alpha/k$, where $\alpha = \pi/NA$, and NA is the numerical aperture of the focused beam. The beam is rotationally scanned so that the signal is sampled for all angles $-\pi \le \theta < \pi$, and the beam is also translated along the y axis to cover all axial coordinates p. Figure 2 illustrates this notation.

In our previous work, it was assumed that the direction of propagation of the beam was fixed to be along the z direction. The location of the center of the beam in the waist
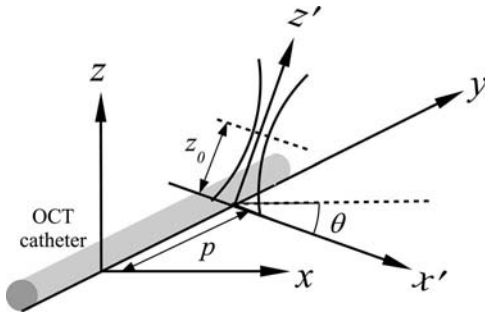
Fig. 2. Geometry of the derivation. A Gaussian beam originates at a position $x=0$, $y=p$, $z=0$, and travels parallel to the $x'-z'$ plane at an angle θ from the x axis. The Gaussian beam is focused so the beam waist is a distance z_0 from the y axis.

plane was given by $\mathbf{r_0}$. Then the signal measured in the interferometer given by the expression $\widetilde{S}(\mathbf{r},k)$ is given by

$$\widetilde{S}(\mathbf{r},k) = i(2\pi)^{-2} A(k) k^{-1} \int_V d^3r\, \eta(\mathbf{r}) f^2(\mathbf{r}-\mathbf{r_0};k), \qquad (2)$$

where $\eta(\mathbf{r})$ is the susceptibility of the sample being probed, and $f^2(\mathbf{r}';k)$ is given by the expression

$$f^2(\mathbf{r}';k) = \frac{1}{(2\pi)^2} \int d^2\xi \exp(-i\boldsymbol{\xi}\cdot\mathbf{r}') \frac{1}{2}\left(\frac{\alpha^2}{k^2} + \frac{i(z'-z_0)}{k}\right)^{-1}$$

$$\times \exp\left(-\frac{\xi^2\alpha^2}{4k^2}\right) \exp[i(z'-z_0)\sqrt{(2k)^2-\xi^2}], \qquad (3)$$

where $\boldsymbol{\xi}=(\xi_x,\xi_y,0)$ and the integral is over the ξ_x, ξ_y plane. Note that, unlike in Ref. 12 we do not make the paraxial approximation for the phase term. In this work, the signal depends on frequency, positions along the y axis, and the angle of propagation of the beam as described above. This signal, $\widetilde{S}(k,p,\theta)$, may be found from Eq. (2) by writing the integrand in the coordinates stationary with respect to the beam. Thus we obtain

$$\widetilde{S}(k,p,\theta) = i(2\pi)^{-2} A(k) k^{-1} \int_V d^3r'\, \eta[\mathbf{R}(\theta)\mathbf{r}'] f^2(\mathbf{r}'-p\hat{\mathbf{y}};k). \tag{4}$$

By substituting Eq. (3) into Eq. (4) and rearranging terms, we find

$$\widetilde{S}(k,p,\theta) = \frac{i}{2} A(k) k^{-1} \int d^2\xi \exp[-iz_0\sqrt{(2k)^2-\xi^2}]$$

$$\times \exp\left(-\frac{\xi^2\alpha^2}{4k^2}\right)$$

$$\times \int d^3r' \exp[-i\boldsymbol{\xi}\cdot(\mathbf{r}'-p\hat{\mathbf{y}})]\eta[\mathbf{R}(\theta)\mathbf{r}']$$

$$\times \left[\frac{\alpha^2}{k^2} + \frac{i(z'-z_0)}{k}\right]^{-1} \exp[iz'\sqrt{(2k)^2-\xi^2}]. \tag{5}$$

In our analysis of the OCT inverse problem on a Cartesian grid, we found that under certain reasonable approximations, the data could be related to the object susceptibility through a resampling scheme in the Fourier

domain.[12] We derive a similar relation here. To do so, it will be advantageous to replace $\left[\frac{\alpha^2}{k^2}+\frac{i(z'-z_0)}{k}\right]$ with an approximation commensurate with the natural geometry of the problem. Explicitly, we replace z' with $\rho'=\sqrt{z'^2+x'^2}$. For most OCT systems, the bandwidth is a small fraction of the central frequency, and so we replace $1/k^2$ with $1/kk_0$. Thus the factor $\left[\frac{\alpha^2}{k^2}+\frac{i(z'-z_0)}{k}\right]$ is replaced by $\frac{1}{k}\left[\frac{\alpha^2}{k_0}+i(\sqrt{x'^2+z'^2}-z_0)\right]$. This expression is slowly varying relative to the rapidly varying phase of the term $\exp[iz'\sqrt{(2k)^2-\xi^2}]$, and so approximations to it tend not to change the result greatly. With this substitution,

$$\widetilde{S}(k,p,\theta) = \frac{i}{2} A(k) \int d^2\xi \exp[-iz_0\sqrt{(2k)^2-\xi^2}] \exp\left(-\frac{\xi^2\alpha^2}{4k^2}\right)$$

$$\times \int d^3r' \exp[-i\boldsymbol{\xi}\cdot(\mathbf{r}'-p\hat{\mathbf{y}})]\eta[\mathbf{R}(\theta)\mathbf{r}']$$

$$\times \left[\frac{\alpha^2}{k_0} + i(\rho'-z_0)\right]^{-1} \exp[iz'\sqrt{(2k)^2-\xi^2}]. \tag{6}$$

To evaluate this integral, we change variables in the inner integral to the coordinates stationary in the reference frame of the sample, $\mathbf{r}'=\mathbf{R}(-\theta)\mathbf{r}$.

$$\widetilde{S}(k,p,\theta) = \frac{i}{2} A(k) \int d^2\xi \exp[-iz_0\sqrt{(2k)^2-\xi^2}]$$

$$\times \exp\left(-\frac{\xi^2\alpha^2}{4k^2}\right) \exp(i\xi_y p)$$

$$\times \int d^3r \exp\{-i[\boldsymbol{\xi}-\hat{\mathbf{z}}\sqrt{(2k)^2-\xi^2}]\cdot\mathbf{R}[(-\theta)\mathbf{r}]\}$$

$$\times \eta(\mathbf{r})\left[\frac{\alpha^2}{k_0} + i(\rho-z_0)\right]^{-1}, \tag{7}$$

where $\rho=\rho'=\sqrt{x^2+z^2}$. It may be seen that the integral over $\mathbf{r}$ results in a Fourier transform if we note that $[\boldsymbol{\xi}-\hat{\mathbf{z}}\sqrt{(2k)^2-\xi^2}]\cdot\mathbf{R}(-\theta)\mathbf{r}=\mathbf{R}(\theta)[\boldsymbol{\xi}-\hat{\mathbf{z}}\sqrt{(2k)^2-\xi^2}]\cdot\mathbf{r}$, after which we obtain

$$\widetilde{S}(k,p,\theta) = \frac{i}{2} A(k) \int d^2\xi \exp[-iz_0\sqrt{(2k)^2-\xi^2}]$$

$$\times \exp\left(-\frac{\xi^2\alpha^2}{4k^2}\right) \exp(i\xi_y p)$$

$$\times \widetilde{\eta}\{-\mathbf{R}(\theta)[\boldsymbol{\xi}-\hat{\mathbf{z}}\sqrt{(2k)^2-\xi^2}]\}, \tag{8}$$

where $\widetilde{\eta}(\beta)$ is the weighted Fourier transform of $\eta(\mathbf{r})$ given by

$$\widetilde{\eta}(\beta) = \int d^3r \exp(i\mathbf{r}\cdot\beta)\eta(\mathbf{r})\left[\frac{\alpha^2}{k_0}+i(\rho-z_0)\right]^{-1}. \tag{9}$$

To change the integral over $\boldsymbol{\xi}$ to a cyclic convolution, we make the substitution $\sqrt{(2k)^2-\xi_y^2}\cos\phi=\xi_x$ so that $\sqrt{(2k)^2-\xi_y^2}\sin\phi=\sqrt{(2k)^2-\xi^2}$, after which we obtain

$$\widetilde{S}(k,p,\theta) = \frac{i}{2}A(k)\int d\xi_y \exp(i\xi_y p)\int_0^\pi d\phi \left\{ [\sqrt{(2k)^2 - \xi_y^2}\sin\phi]\right.$$

$$\times \exp[-iz_0\sqrt{(2k)^2 - \xi^2}]\exp\left(-\frac{\xi^2\alpha^2}{4k^2}\right)\right\}$$

$$\times \widetilde{\eta}\{-\mathbf{R}(\theta)[\hat{\mathbf{x}}\cos\phi\sqrt{(2k)^2 - \xi_y^2}$$

$$+ \hat{\mathbf{y}}\xi_y - \hat{\mathbf{z}}\sin\phi\sqrt{(2k)^2 - \xi_y^2}]\}. \tag{10}$$

For brevity, we define the kernel function $K(k,\xi_y,\phi)$:

$$K(k,\xi_y,\phi) = \frac{i}{2}A(k)[\sqrt{(2k)^2 - \xi_y^2}\sin\phi]$$

$$\times \exp[-iz_0\sqrt{(2k)^2 - \xi^2}]\exp\left(-\frac{\xi^2\alpha^2}{4k^2}\right). \tag{11}$$

We note that the $\cos\phi$ next to $\hat{\mathbf{x}}$ and the $\sin\phi$ next to $\hat{\mathbf{z}}$ in Eq. (10) effect a rotation in the x–z plane through an angle $-\phi$ of a vector $\hat{\mathbf{x}}\sqrt{(2k)^2 - \xi_y^2}$. Given this, we can express Eq. (10) as a cyclic convolution:

$$\widetilde{S}(k,p,\theta) = \int d\xi_y \exp(i\xi_y p)\int_0^\pi d\phi K(k,\xi_y,\phi)$$

$$\times \widetilde{\eta}\{-\mathbf{R}(\theta - \phi)[\hat{\mathbf{x}}\sqrt{(2k)^2 - \xi_y^2} + \hat{\mathbf{y}}\xi_y]\}. \tag{12}$$

By combining the rotations $\mathbf{R}(\theta)$ and $\mathbf{R}(-\phi)$, we find that the integral over ϕ is a cyclic convolution. This cyclic convolution can be performed efficiently using the product of Fourier series coefficients. To put Eq. (10) into diagonal form, we define the following functions of the data, the kernel, and the structure function:

$$\widetilde{\widetilde{S}}(k,\xi_p,n_0) = \int_{-\infty}^\infty \int_{-\pi}^\pi dp\, d\theta \exp(ip\xi_p)\exp(i\theta n_\theta)\widetilde{S}(k,p,\theta),$$

$$\tag{13}$$

$$\widetilde{K}(k,\xi_y,n_\theta) = \int_0^\pi d\theta \exp(i\theta n_\theta)K(k,\xi_y,\theta), \tag{14}$$

$$\widetilde{\widetilde{\eta}}(k,\xi_y,n_\theta) = \int_{-\pi}^\pi d\theta \exp(i\theta n_\theta)\widetilde{\eta}\{-[\hat{\mathbf{x}}\cos\theta\sqrt{(2k)^2 - \xi_y^2}$$

$$+ \hat{\mathbf{y}}\xi_y + \hat{\mathbf{z}}\sin\theta\sqrt{(2k)^2 - \xi_y^2}]\}, \tag{15}$$

where n_θ is an integer on $[-\infty,\infty]$. If we insert the definitions of Eqs. (13)–(15) into Eq. (12), we find the following relationship:

$$\widetilde{\widetilde{S}}(k,\xi_p,n_\theta) = \widetilde{K}(k,\xi_p,n_\theta)\widetilde{\widetilde{\eta}}(k,\xi_p,n_\theta). \tag{16}$$

In this form we see that $\widetilde{\widetilde{S}}$ and $\widetilde{\widetilde{\eta}}$ are related by a diagonal integral operator whose kernel is $\widetilde{K}(k',\xi_p',n_\theta')\delta(k-k')$ $\times \delta(\xi_p - \xi_p')\delta_{n_\theta n_\theta'}$. Explicitly $\widetilde{\widetilde{\mathbf{S}}} = \widetilde{\mathbf{K}}\widetilde{\widetilde{\boldsymbol{\eta}}}$ where $\widetilde{\mathbf{K}}$ is the integral operator:

$$[\widetilde{\mathbf{K}}\widetilde{\widetilde{\boldsymbol{\eta}}}](k,\xi_p,n_\theta) = \int dk'\int d\xi_p'\sum_{n_\theta}\widetilde{K}(k',\xi_p',n_\theta')\delta(k-k')$$

$$\times \delta(\xi_p - \xi_p')\delta_{n_\theta n_\theta'}\widetilde{\widetilde{\eta}}(k',\xi_p',n_\theta'). \tag{17}$$

This diagonal operator will simplify finding solutions to specific inverse problems.

3. INVERSE PROBLEM

Equation (16) defines a linear relationship between the object structure and the data. To better understand how to invert this relationship, the relationship between the data $\widetilde{S}(k,p,\theta)$ and the object $\eta(\mathbf{r})$ is written explicitly:

$$\widetilde{S}(k,p,\theta) = \frac{1}{4\pi^2}\int d\xi_y \exp(-i\xi_y p)$$

$$\times \sum_{n_\theta=-\infty}^\infty \exp(-i\theta n_\theta)K(k,\xi_y,n_\theta)$$

$$\times \int d^3r\,\eta(\mathbf{r})\left[\frac{\alpha^2}{k_0} + i(\rho - z_0)\right]^{-1}$$

$$\times \int_{-\pi}^\pi d\phi \exp(i\phi n_\theta)\exp\{-i\mathbf{r}\cdot\mathbf{R}(\phi)$$

$$\cdot [\hat{\mathbf{x}}\sqrt{2(k)^2 - \xi_y^2} + \hat{\mathbf{y}}\xi_y]\}, \tag{18}$$

where $\widetilde{K}(k,\xi_p,n_\theta)$ is given explicitly by

$$\widetilde{K}(k,\xi_p,n_\theta) = \frac{i}{2}A(k)\int_0^\pi d\theta \exp(i\theta n_\theta)$$

$$\times \exp\left[-\frac{(2k)^2\cos^2\theta + \xi_p^2\sin^2\theta}{2}\frac{\alpha^2}{2k^2}\right]$$

$$\times \exp[-iz_0\sin\theta\sqrt{(2k)^2 - \xi_p^2}]$$

$$\times \sqrt{(2k)^2 - \xi_p^2}\sin\theta. \tag{19}$$

Equation (18) can be rewritten to use a Fredholm-type kernel $\kappa(k,p,\theta,\mathbf{r})$ such that

$$S(k,p,\theta) = \boldsymbol{\kappa}\boldsymbol{\eta} = \int d^3r\kappa(k,p,\theta,\mathbf{r})\eta(\mathbf{r}). \tag{20}$$

Although Eq. (20) may not be strictly solvable, a least-squares solution $\boldsymbol{\eta}^+$ can be found by minimizing a functional:

$$\boldsymbol{\eta}^+ = \arg\min_{\boldsymbol{\eta}}|\mathbf{S} - \boldsymbol{\kappa}\boldsymbol{\eta}|^2$$

$$= \arg\min_{\eta}\int_0^\infty dk\int_{-\infty}^\infty dp\int_{-\pi}^\pi d\theta|S(k,p,\theta)$$

$$- \boldsymbol{\kappa}\eta(\mathbf{r})|^2. \tag{21}$$

The least-squares solution is then given by the pseudoinverse $\boldsymbol{\eta}^+ = (\boldsymbol{\kappa}^\dagger\boldsymbol{\kappa})^{-1}\boldsymbol{\kappa}^\dagger\mathbf{S}$. While this solution is formally correct, the inverse $(\boldsymbol{\kappa}^\dagger\boldsymbol{\kappa})^{-1}$ can be difficult to compute in practice. Instead, we find the least-squared error solution

for the weighted Fourier transform $\widetilde{\boldsymbol{\eta}}^+$ that, while not directly minimizing the error relative to the measurements, still constrains the estimated object structure to be consistent with the data:

$$\widetilde{\boldsymbol{\eta}}^+ = \arg\min_{\widetilde{\widetilde{\boldsymbol{\eta}}}} |\widetilde{\widetilde{\mathbf{S}}} - \mathbf{K}\widetilde{\widetilde{\boldsymbol{\eta}}}|^2 + \lambda |\widetilde{\widetilde{\boldsymbol{\eta}}}|^2$$

$$= \arg\min_{\widetilde{\widetilde{\boldsymbol{\eta}}}} \int_0^\infty dk \int_{-\infty}^\infty d\xi_p \sum_{n_\theta=-\infty}^\infty |\widetilde{\widetilde{S}}(k,\xi_p,n_\theta)$$

$$- K(k,\xi_p,n_\theta)\widetilde{\widetilde{\eta}}(k,\xi_p,n_\theta)|^2 + \lambda |\widetilde{\widetilde{\eta}}(k,\xi_p,n_\theta)|^2. \quad (22)$$

This least-squares solution keeps the object estimate consistent with Eq. (16). Also included is a Tikhonov regularization term to stabilize the solution, with regularization parameter λ. The solution $\widetilde{\widetilde{\eta}}^+$ is

$$\widetilde{\widetilde{\eta}}^+(k,\xi_p,n_\theta) = \frac{\widetilde{\widetilde{S}}(k,\xi_p,n_\theta)K^*(k,\xi_p,n_\theta)}{|K(k,\xi_p,n_\theta)|^2 + \lambda}. \quad (23)$$

This least-squares solution is a numerically simpler method of estimating the object structure. Starting with data given by $S(k,p,\theta)$, we can compute $\widetilde{\widetilde{S}}(k,\xi_p,n_\theta)$ by using Eq. (13). Using Eq. (23) one can compute $\widetilde{\widetilde{\eta}}^+(k,\xi_p,n_\theta)$. Then Eq. (15) can be solved for $\widetilde{\eta}^+$ by taking the discrete inverse Fourier transform of $\widetilde{\widetilde{\eta}}^+$ with respect to n_θ. Finally, a 3D inverse Fourier transform computes $\eta^+(\mathbf{r})$ from $\widetilde{\eta}^+$. In the limit that $\lambda \to 0$ and all data are continuously available, this approach yields an exact solution for $\eta(\mathbf{r})$. In the more realistic case that a regularized solution is employed, a stable solution is obtained.

4. SIMULATION

To demonstrate the algorithm, we implemented a simulation of the forward and inverse scattering in the radial OCT geometry. A synthetic object was created comprised of pointlike scatterers. The simulated OCT data were calculated from the exact forward problem by using Eq. (4), and then the regularized solution of the inverse scattering solution was calculated by using Eq. (23). The simulation is of a pseudo-3D object that is invariant along the y axis, so that the object is effectively 2-D.

The simulation was performed with lengths in units of the central wavelength of the illumination. Typical center wavelengths for OCT imaging are between 800 and 1400 nm. The cross section of the simulated object was taken to be approximately 135 by 135 λ. The Gaussian illumination beam was assumed to be focused 45 λ from the origin, with a beam waist width of 2.5 λ. The scatterers were placed 15–60 λ from the origin at randomly selected angles relative to the x axis. The simulated source was taken to have a Gaussian spectrum with a FWHM fractional bandwidth of approximately 25%. Each of the scatterers had the same susceptibility.

The forward-scattering problem was implemented by directly summing the contribution of each point scatterer individually by using Eq. (4). This was achieved by summing for each sampled data point $\widetilde{S}(k,\theta)$ the total col-

lected backscattered amplitude for all of the scatterers at their respective positions $\mathbf{r}'$, the amplitude $f^2(\mathbf{r}';k)$, as specified in Eq. (3). Note that in Eq. (3) the exact phase rather than the Fresnel quadratic approximation was used to more accurately compute the data for a high-NA beam. To show the equivalent OCT image, the data were inverse Fourier transformed along the k axis, yielding $S(r,\theta)$. The resulting $S(r,\theta)$ is displayed in a polar plot in Fig. 3(a). The dotted circle in the diagram indicates the radius at which the Gaussian beam is focused. Note that the images of points located closer to the origin than the focus (inside the circle) curve toward the origin, and the points located further from the origin than the focus curve (outside the circle) away from the origin, as would be expected.

The inverse scattering problem was implemented by using the approximate solution embodied in Eq. (23). The data are given as $\widetilde{S}(k,\theta)$. To utilize Eq. (23), several Fourier-transform steps were needed. The inverse scattering algorithm was implemented by using the following steps:

1. The data $\widetilde{S}(k,\theta)$ were Fourier transformed with respect to θ to yield $\widetilde{\widetilde{S}}(k,n_\theta)$.

2. The function $\widetilde{K}(k,\theta)$ was calculated (using $\xi_p=0$) and then Fourier transformed with respect to θ to yield $\widetilde{K}(k,n_\theta)$ as per Eq. (19).
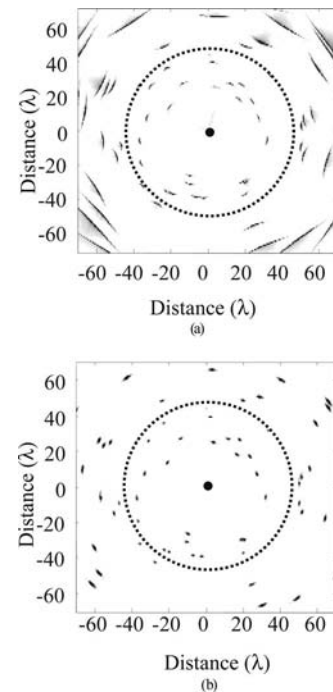

Fig. 3.   Simulated and reconstructed OCT catheter images. The simulated area is 135 by 135 λ, and the Gaussian beam has a 2.5 λ beam waist, focused 45λ from the origin. (a) Simulated OCT data for randomly scattered point objects. The dotted circle coincides with the focus radius of the Gaussian beam, and the dark center represents the location of the OCT catheter. Points inside the circle have wavefronts that curve toward the origin, and points outside the circle have wavefronts that curve away from the origin. (b) Reconstruction of the point sources from the simulated data.

3. The regularized $\widetilde{\widetilde{\eta}}^+(k, n_\theta)$ was calculated by using Eq. (23).

4. $\widetilde{\widetilde{\eta}}^+(k, n_\theta)$ was inverse Fourier transformed with respect to n_θ to yield $\widetilde{\eta}^+(k, \theta)$.

5. The $\widetilde{\eta}^+(k, \theta)$ was inverse Fourier transformed with respect to k to yield $\eta_R^+(l, \theta)$, the Radon transform of $\eta^+(x, z)$.

6. The inverse Radon transform of $\eta_R^+(l, \theta)$ was performed to yield $\eta^+(x, z)$, the Tikhonov-regularized inverse.

The inverse Radon transform was used as a convenient way to convert from the polar representation of the Fourier transform $\widetilde{\eta}^+(k, \theta)$ to its inverse Fourier-transform Cartesian counterpart $\eta^+(x, z)$, using the Fourier projection slice theorem. Unfortunately, many implementations of the inverse Radon transform, such as the filtered backprojection method that was used for this simulation, are slow, and therefore care will need to be exercised to ensure that the computational burden is not too great. Methods exist to implement the inverse Radon transform in $O(N^2 \log N)$ time,[25,26] rather than the $O(N^3)$ typical of most filtered backprojection inverse Radon transform methods.

The results of the inverse scattering computation are shown in Fig. 3(b). As can be seen, the blurred arcs corresponding to the point sources in the uncorrected OCT data are corrected to be pointlike when inverse scattering is performed on the data. The algorithm correctly compensates for the range-dependent blur and curvature of the backscattered signal. Unlike in our previous work,[12] the reconstructed image does not exhibit uniform resolution. The resolution of the reconstruction depends on the distance from the origin. Because the beam width is wide near the origin, points nearer the origin than the focus are overlapped by the beam for many angles θ, so that the resolution of points near the origin is high. At the focus, the beam width is narrow and so the points near the focus are also well resolved. Far from the origin, the beam is wide and points are overlapped only by the beam for a narrow range of angles given by the divergence of the beam, so that the resolution degrades with distance from the origin. Generally, the resolution is nearly constant between the origin and the focus radius, and slowly degrades to a constant angular resolution at radii further than the focus. Therefore the most useful resolution will be achieved for distances at or closer than the focus radius.

To explore the range-dependent resolution further, we show a simulation of point scatterers reconstructed with beams with various widths and focus radii. Figure 4 has four parts, each of which is the simulated resolution of point scatterers for beams of different widths. The number next to each curve is the focus radius for each simulated beam. The resolution is measured as the FWHM of the reconstructed point in the angular direction. Each graph relates the FWHM resolution to the distance from the axis to the simulated point. For small beam waists, as in Figs. 4(a)–4(c), the resolution is approximately constant for radii closer than the focus radius. Further from the focus the FWHM resolution starts to increase. For the wider beams, the transverse resolution near the origin
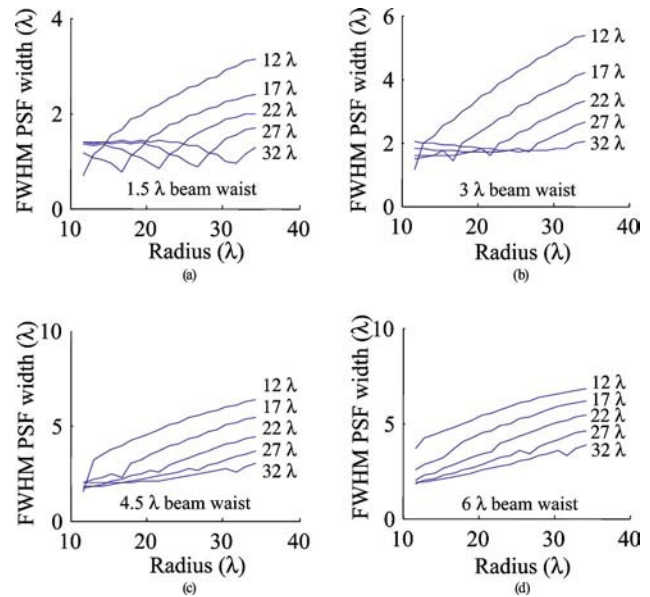

Fig. 4. (Color online) Resolution chart showing FWHM transverse point-spread-function (PSF) resolution of simulated point sources situated at difference distances from the catheter axis, as a function of focus radius and beam width. The abscissa is the distance from the origin from which the simulated point source is placed. In each part, the number next to each curve is the distance away from the origin from which the beam was focused. The beam waist for each part is (a) 1.5 λ, (b) 3 λ, (c) 4.5 λ, (d) 6 λ.
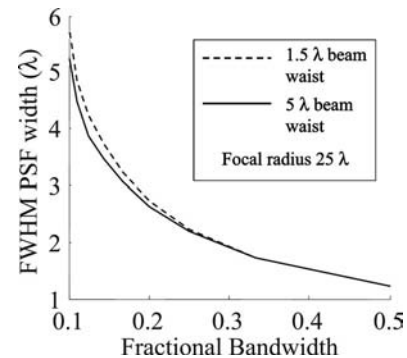

Fig. 5. Resolution chart showing FWHM axial resolution of simulated point sources imaged with two different beam widths focused 25 λ from the catheter axis, for various fractional bandwidths of the source. The dotted curve corresponds to a 1.5 λ beam waist, and the solid curve corresponds to a 5 λ beam waist. PSF, point-spread function.

can be somewhat better than the width of the beam waist. In the future, a closed-form expression for the range-dependent resolution may be possible.

To examine the validity of the approximation made in Eq. (6) of small fractional bandwidth, we simulate the reconstruction of point scatterers imaged with various source bandwidths. The simulated focus radius is 25 λ, and the beam widths are 1.5 and 5 λ. Figure 5 shows the FWHM axial resolution as a function of fractional bandwidth. The resolution should be approximately half of the reciprocal of the fractional bandwidth, to which the simulation conforms.

There are several other factors that can influence the practical limits of resolution that are not addressed here. This derivation accounts only for single scattering, which

is a standard assumption in OCT, but one that is likely not to hold in sufficiently scattering tissues (e.g., the high-index mismatch of the air–tissue boundary of alveoli in the lungs). The index of refraction of the medium can vary in tissue, sometimes up to 10% between water and lipids, for example, which may introduce refraction of the beam that can distort the image as well. In addition, the catheter may wobble as it is rotated around its axis, so that there will be error in the focal radius. Finally, the optical phase of the interference must be measured reliably, so features in the tissue must be ranged to an accuracy of a fraction of a wavelength. While we believe these problems are solvable, they may present an impediment to realizing the proposed resolution gains.

We have derived and demonstrated an algorithm that infers the susceptibility of a scatterer from the signal acquired in angularly scanned OCT. These results will be useful in catheter-based OCT and perhaps in endoscopic or intravascular ultrasound as well. Other applications could include acoustic, sonar, and seismic sensing where the imaged object is close to a focused transducer as well as radar, microwave, and terahertz wave sensing of objects near a rotating dish antenna.

ACKNOWLEDGMENTS

REFERENCES

1. D. Huang, E. A. Swanson, C. P. Lin, J. S. Schuman, W. G. Stinson, W. Chang, M. R. Hee, T. Flotte, K. Gregory, C. A. Puliafito, and J. G. Fujimoto, "Optical coherence tomography," Science **254**, 1178–1181 (1991).
2. B. E. Bouma and G. J. Tearney, eds., *Handbook of Optical Coherence Tomography* (Marcel Dekker, 2001).
3. G. J. Tearney, M. E. Brezinski, B. E. Bouma, S. A. Boppart, C. Pitris, and J. F. Southern, "In vivo endoscopic optical biopsy with optical coherence tomography," Science **276**, 2037–2039 (1997).
4. A. M. Rollins, R. Ung-arunyawee, A. Chak, R. C. K. Wong, K. Kobayashi, M. V. Sivak, Jr., and J. A. Izatt, "Real-time *in vivo* imaging of human gastrointestinal ultrastructure by use of endoscopic optical coherence tomography with a novel efficient interferometer design," Opt. Lett. **24**, 1358–1360 (1999).
5. F. I. Feldchtein, G. V. Gelikonov, V. M. Gelikonov, R. V. Kuranov, A. M. Sergeev, N. D. Gladkova, A. V. Shakhov, N. M. Shakhova, L. B. Snopova, A. B. Terent'eva, E. V. Zagainova, Y. P. Chumakov, and I. A. Kuznetova, "Endoscopic applications of optical coherence tomography," Opt. Express **3**, 257–270 (l998).
6. V. X. D. Yang, M. L. Gordon, S.-J. Tang, N. E. Marcon, G. Gardiner, B. Qi, B. Stuart, E. Seng-Yue, S. Lo, J. Pekar, B. C. Wilson, and V. I. Vitkin, "High speed, wide velocity dynamic range Doppler optical coherence tomography (Part iii): *in vivo* endoscopic imaging on blood flow in the rat and human gastrointestinal tracts," Opt. Express **11**, 2416–2424 (2003).
7. G. J. Tearney, S. A. Boppart, B. E. Bunma, M. E. Brezinski, N. J. Weissman, J. F. Southern, and J. G. Fujimoto, "Scanning single-mode fiber-optic catheter endoscope for optical coherence tomography," Opt. Lett. **21**, 543–545 (1996).
8. X. Li, T. H. Ko, and J. G. Fujimoto, "Intraluminal fiber-optic Doppler imaging catheter for structural and functional optical coherence tomography," Opt. Lett. **26**, 1906–1908 (2001).
9. P. R. Herz, Y. Chen, A. D. Aguirre, K. Schneider, P. Hsuing, J. G. Fujimoto, K. Madden, J. Schmitt, J. Goodnow, and C. Petersen, "Micromotor endoscope catheter for *in vivo*, ultrahigh resolution optical coherence tomography," Opt. Lett. **29**, 2261–2263 (2004).
10. B. E. Bouma and G. J. Tearney, "Power-efficient nonreciprocal interferometer and linear-scanning fiber-optic catheter for optical coherence tomography," Opt. Lett. **24**, 531–533 (1999).
11. I. K. Jang, B. E. Bouma, D. H. Kang, S. J. Park, S. W. Park, K. B. Seung, K. B. Choi, M. Shishkov, K. Schlendorf, E. Pomerantsev, S. L. Houser, and H. T. Aretz, "Visualization of coronary atherosclerotic plaques in patients using optical coherence tomography: comparison with intravascular ultrasound," J. Am. Coll. Cardiol. **39**, 604–609 (2002).
12. T. S. Ralston, D. L. Marks, P. S. Carney, and S. A. Boppart, "Inverse scattering problem for optical coherence tomography," J. Opt. Soc. Am. A **23**, 1027–1037 (2006).
13. B. E. Bouma, G. J. Tearney, H. Yabushita, M. Shishkov, C. R. Kauffman, D. DeJoseph Gauthier, B. D. MacNeill, S. L. Houser, H. T. Aretz, E. F. Halpern, and I. K. Jang, "Evaluation of intracoronary stenting by intravascular optical coherence tomography," Heart **89**, 317–320 (2003).
14. B. D. MacNeill, B. E. Bouma, H. Yabushita, I. K. Jang, and G. J. Tearney, "Intravascular optical coherence tomography: cellular imaging," J. Nucl. Cardiol. **12**, 460–465 (2005).
15. I. K. Jang, G. J. Tearney, B. MacNeill, M. Takano, F. Moselewski, N. Iftima, M. Shishkov, S. Houser, H. T. Aretz, E. F. Halpern, and B. E. Bouma, "In vivo characterization of coronary atherosclerotic plaque by use of optical coherence tomography," Circulation **111**, 1551–1555 (2005).
16. M. A. Haun, D. L. Jones, and W. D. O'Brien, Jr., "Efficient three-dimensional imaging from a small cylindrical aperture," IEEE Trans. Ultrason. Ferroelectr. Freq. Control **49**, 861–870 (2002).
17. S. J. Norton and M. Linzer, "Ultrasonic reflectivity imaging in three dimensions: exact inverse scattering solutions for plane, cylindrical, and spherical apertures," IEEE Trans. Biomed. Eng. **BME-28**, 202–220 (1981).
18. C. J. Nolan and M. Cheney, "Synthetic aperture inversion," Inverse Probl. **18**, 221–235 (2002).
19. H. Hellsten and L. E. Andersson, "An inverse method for the processing of synthetic aperture radar data," Inverse Probl. **3**, 111–124 (1987).
20. L. M. H. Ulander, H. Hellsten, and G. Stenstrom, "Synthetic aperture radar processing using fast factorized back-projection," IEEE Trans. Aerosp. Electron. Syst. **39**, 760–776 (2003).
21. J. A. Fawcett, "Inversion of N-dimensional spherical averages," SIAM J. Appl. Math. **45**, 336–341 (1985).
22. C. H. Frazier and W. D. O'Brien, Jr., "Synthetic aperture techniques with a virtual source element," IEEE Trans. Ultrason. Ferroelectr. Freq. Control **45**, 196–207 (l998).
23. K. J. Langenberg, M. Berger, T. Kreutter, K. Mayer, and V. Schmitz, "Synthetic aperture focusing technique signal processing," NDT Int. **19**, 177–189 (1986).
24. D. Vray, C. Haas, T. Rastello, M. Krueger, E. Brusseau, K. Schroeder, G. Gimenez, and H. Ermert, "Synthetic aperture-based beam compression for intravascular ultrasound imaging," IEEE Trans. Ultrason. Ferroelectr. Freq. Control **48**, 189–201 (2001).
25. P. Edholm and G. T. Herman, "Linograms in image reconstruction from projections," IEEE Trans. Med. Imaging **MI-6**, 301–307 (1987).
26. S. Basu and Y. Bresler, "O(N2 log2N) filtered backprojection reconstruction algorithm for tomography," IEEE Trans. Image Process. **9**, 1760–1773 (2000).